Mesoscopic-scale simulation of pore evolution during laser powder bed fusion process

Liu Cao

Advanced Institute of Engineering Science for Intelligent Manufacturing, Guangzhou University, Guangzhou 510006, Guangdong, PR China

ABSTRACT

Laser powder bed fusion (LPBF) is an advanced manufacturing technology that uses data-driven, layer-by-layer accumulation of materials to form metal components and has been widely applied in aerospace and other fields. Effectively controlling pore defects is a key scientific problem and technical difficulty in LPBF industrial production. Based on the open-source discrete element method code Yade, the particle distribution of the powder bed was obtained. Based on the open-source computational fluid dynamics code OpenFOAM, the pore evolution during the LPBF formation process at the mesoscopic scale was predicted. The thermal–force factors affecting the molten pool included the surface tension, Marangoni effect, gasification recoil force, and mushy drag force. The laser energy model used a body heat source based on interface tracking. First, dimensionless analysis of the molten pool evolution in the case of LPBF single-track formation was carried out. The molten pool evolution was mainly influenced by the gasification recoil force, Marangoni effect and surface tension, and the main influencing factors on different zones of the molten pool were different. To examine the influences of the laser power, scanning speed, powder bed thickness, and hatch space on the pore defect in the LPBF formation process, simulations were carried out and compared with experimental results. When the volumetric energy density was too small, pore defects occurred due to insufficient fusion of metal particles, and when the volumetric energy density was too large to cause the "keyhole" effect, pore defects occurred because the entrained gas could not escape in time. This paper is expected to provide theoretical guidance for the scientific regulation of pore defects in LPBF production.

1. Introduction

Laser powder bed fusion (LPBF) is an advanced manufacturing technology that uses data-driven, layer-by-layer accumulation of a material to form metal components. It uses a laser beam to selectively act on a powder bed and has been widely applied in the aerospace, biomedical, and other fields [1]. The scanning of the powder bed by the laser beam to melt and deposit is a complex process in which multiple types of physics are coupled and highly dynamic, and the components are prone to macroscopic defects, including warpage, ball, cracking, and internal metallurgical defects, such as pore and slag inclusion [2]. Among these, the pore defect is most affected by the process parameters [3], which can easily cause fatigue cracks [4]. Furthermore, it is difficult to eliminate pores by post-treatment methods such as heat treatment and hot isostatic pressing, which makes pores one of the key defects to be controlled during LPBF production [5].

The pore evolution during the LPBF formation process occurs in a rapidly changing liquid–solid–gas coupled environment at a high temperature. Scholars have conducted many experimental studies on the *in-situ* observation of pores [6–8], the influence of the process parameters on pores [9], the influence of pores on components' mechanical properties [10], and the corrosion behaviors caused by pores [11]. Hojjat-zadeh *et al.* [12] studied the motion and elimination mechanism of pores during the LPBF process by means of *in-situ*, high-speed, high-resolution synchrotron X-ray imaging experiments and found that the pores in the laser interaction region escaped from the molten pool under the high thermocapillary force. Imani *et al.* [13] used in-process layer-by-layer optical images to study the influences of the laser power, scanning speed, and hatch space on the pore defect of LPBF components and found that reducing the laser power by half could lead to a seven-fold increase in the number of pores. The current experimental results have provided a good basis for understanding the evolution mechanism of pore defects during the LPBF process.

As a high-efficiency and low-cost technology for the quantitative analysis of physical processes, numerical simulations have been widely used in recent years to predict temperature, molten pool, stress, microstructure and other information during the LPBF process [14–18]. Since the complex evolution behaviors of pores mainly occur in the
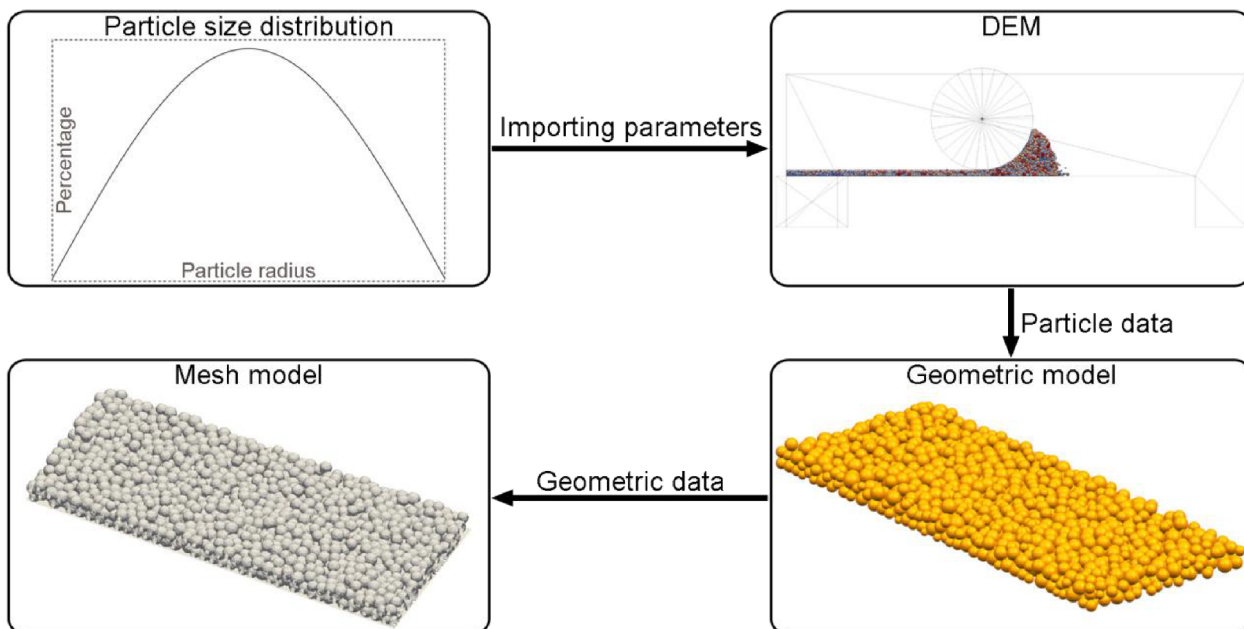
Fig. 1. Flow chart for calculating the particle distribution of the powder bed.
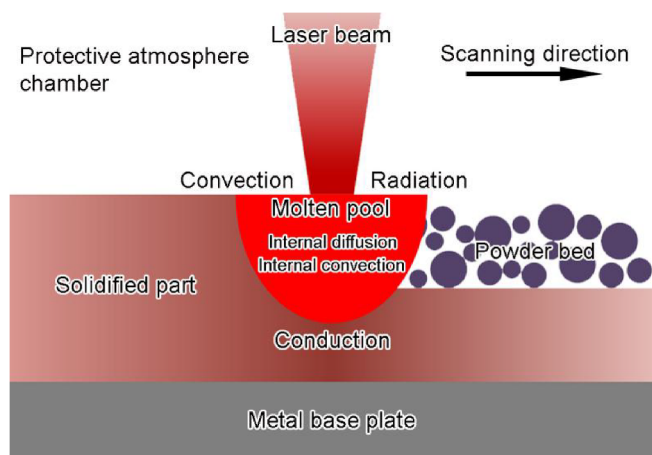

Fig. 2. Schematic diagram of the LPBF formation process.

molten pool, the size of the molten pool in the LPBF process is often on the micrometer scale (mesoscopic scale) [19], so that the pore defect can be effectively described only based on the mesoscopic scale [20,21]. Simulation methods based on the mesoscopic scale involve directly predicting the formation and evolution of pores by describing a series of molten pool dynamic behaviors, such as melting, gasification and solidification of metal particles under laser action [22,23]. At present, the mesoscopic-scale simulation studies of the LPBF process mainly involve two aspects: the particle distribution of the powder bed [24,25] and the molten pool dynamics [26–34]. Han *et al.* [35] used the discrete element method (DEM) to analyze the effect of different powder bed thicknesses on the powder bed quality and found that lower and higher powder bed thicknesses would result in large voids and short-feed defects, respectively. Tang *et al.* [36] predicted the LPBF formation process based on the open-source computational fluid dynamics (CFD) code OpenFOAM and analyzed the effects of the gasification recoil force and surface-tension-induced wetting behavior on the pore defect. Bayat *et al.* [37,38] used a combination of numerical simulations and experiments to study the mechanism of pore defect formation caused by "keyhole" and lack-of-fusion in the LPBF process. The current simulation results provide a good technical basis for

predicting pore defects in the LPBF process, but systematic research on the evolution of pores is lacking, especially the influence of various process parameters on pore defects.

In this paper, the particle distribution of the powder bed was determined by the DEM, and the pore evolution during the LPBF process was predicted at the mesoscopic scale using OpenFOAM. First, the evolution process of the molten pool in the case of LPBF single-track formation was predicted, and the corresponding dimensionless analysis was performed. To examine the influence of different process parameters on pore defects, corresponding simulations were then carried to examine the effects of the laser power, scanning speed, powder bed thickness, and hatch space, and the results were compared with experimental results. This paper is expected to provide theoretical guidance for the scientific regulation of pore defects in the LPBF production.

2. Physical modeling and numerical solution

2.1. Particle distribution of powder bed

The premise of studying the pore evolution in the LPBF process on the mesoscopic scale is to obtain the particle distribution of the powder bed, and its calculation is divided into two parts: determining the particle size distribution and determining the spreading distribution. The particle size distribution must be measured by an experimental method (such as laser particle sizer), and then a specific distribution curve (such as a Gaussian distribution) is used for fitting [39]. The spreading distribution is based on the obtained particle size distribution and is calculated by the Lagrangian algorithm. The most widely used calculation algorithm for spreading powder is the DEM, and the core idea is to study individual particles as the research object. The normal and tangential contact between the particles and the forces between particles and the roller or scraper were considered, and the particle motion and position were updated to obtain the particle distribution [40]. Fig. 1 shows the flow chart for calculating the particle distribution of the powder bed used herein. The particle size distribution was Gaussian, and the spreading distribution was calculated using the open-source DEM code Yade [41]. The particle center and radius data were then imported into 3D modeling software to obtain the geometric model, and finally, pre-processing software was used to obtain the mesh
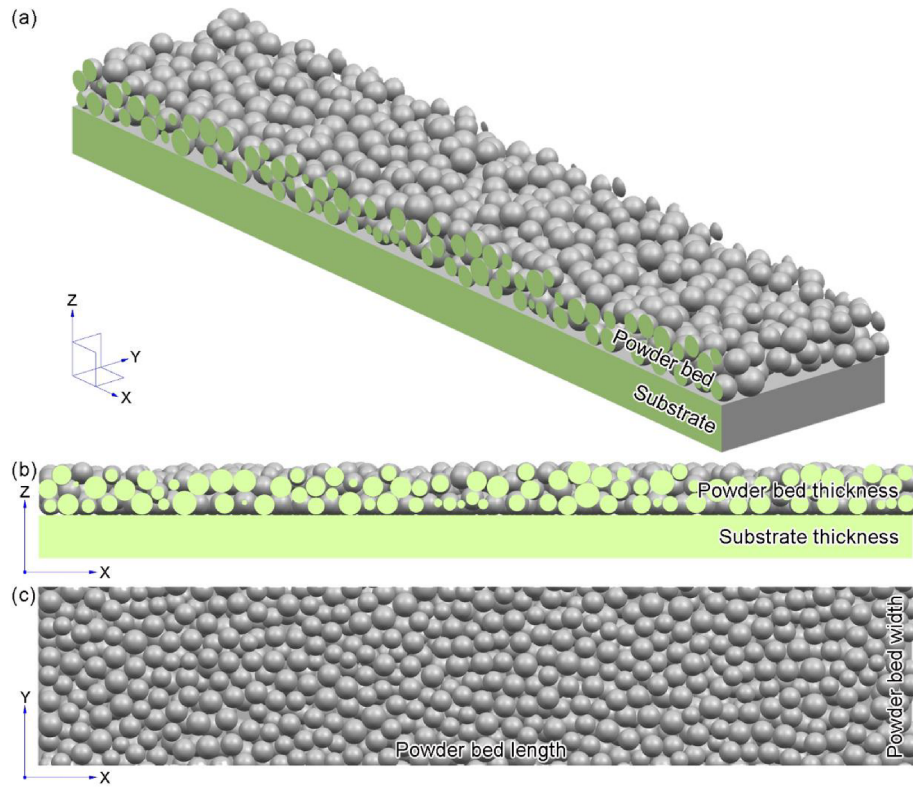
Fig. 3. Geometric model used in LPBF calculation.

Table 1
Required material properties.

Parameter	Value	Unit
Density of metal	7270	kg/m^3
Specific heat of metal	790	J/(kg·K)
Thermal conductivity of metal	24.55	W/(m·K)
Solidus temperature	1658	K
Liquidus temperature	1723	K
Evaporation temperature	3090	K
Latent heat of melting	2.7×10^5	J/kg
Latent heat of vaporization	7.45×10^6	J/kg
Viscosity of liquid metal	0.00345	Pa·s
Surface tension	1.6	N/m
Temperature-dependent coefficient of surface tension	-8×10^{-4}	N/(m·K)
Molar mass	5.593×10^{-2}	kg/mol
Ambient pressure	101,325	Pa
Boltzmann constant	1.380649×10^{-23}	J/K
Emissivity	0.26	
Stefan-Boltzmann constant	5.67×10^{-8}	W/(m^2·K^4)
Density of air	1	kg/m^3
Specific heat of air	718	J/(kg·K)
Thermal conductivity of air	0.02346	W/(m·K)
Viscosity of air	1.48×10^{-5}	Pa·s

Table 2
Laser processing parameters.

Parameter	Value	Unit
Laser spot diameter	54	μm
Scanning speed	1.5	m/s
Laser power	250	W
Absorption coefficient	0.35	

model required for the simulation. The particles were considered to be spherical, and the particle contact force model was the soft ball model [25]. The particle density was set to 7270 kg/m^3, the contact friction angle was set to 0.3, Poisson's ratio was set to 0.34, Young's modulus was set to 195 GPa, and the other parameters were the default Yade settings.

2.2. Prediction model of pore defects

After obtaining the particle distribution of the powder bed, a corresponding numerical algorithm can be used to calculate the pore evolution during the LPBF formation process. The LPBF process contains complex thermal–force couplings and involves factors including the surface tension, Marangoni effect, gasification recoil force, viscous force, mushy drag force, and gravity. Fig. 2 shows the heat exchange pathways that occur during the LPBF process. To ensure the feasibility and efficiency of the numerical calculations, the following three assumptions were made: the flow behaviors of the liquid metal and gas were regarded as laminar flows of incompressible, Newtonian fluids, the mass loss caused by vaporization of the molten metal was ignored, and the influence of the density change on the volume was negligible.

To directly describe the evolution behaviors of the pores, a two-phase flow calculation model was used. In this model, the volume fraction factor α_1 represents the volume fraction of the metal-phase in the element, and the value is between 0 and 1. The governing equations for α_1 are as follows [42]:

$$\frac{\partial \alpha_1}{\partial t} + \nabla \cdot (\alpha_1 \vec{u}) = 0 \tag{1}$$

$$\alpha_1 + \alpha_2 = 1 \tag{2}$$

where α_1 and α_2 are the volume fractions of the metal and gas phases in the element, respectively; t is the time, s; and $\vec{u}$ is the velocity, m/s.
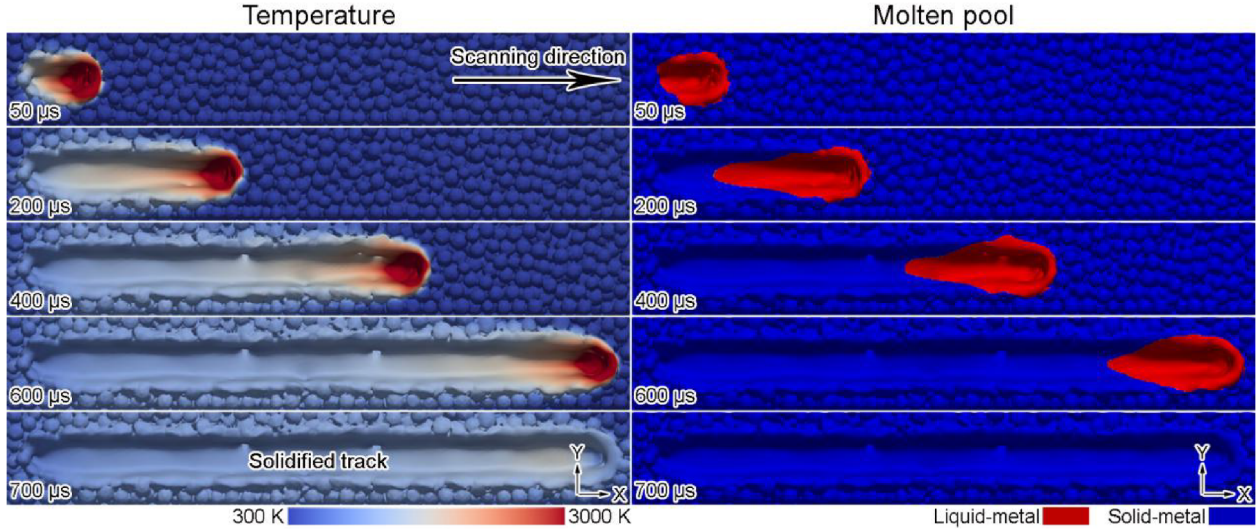
Fig. 4. Top view of the temperature and molten pool distributions at different times.
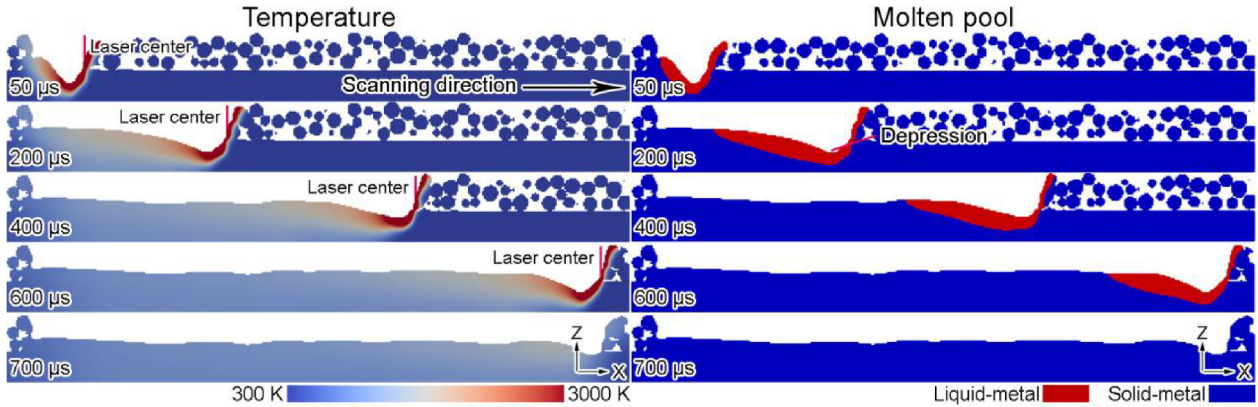

Fig. 5. Mid-sectional view of the temperature and molten pool distributions at different times.

The equations of conservation of momentum, energy, and mass are as follows:

$$\frac{\partial \overline{\rho}\vec{u}}{\partial t} + \nabla\cdot(\overline{\rho}\vec{u} \otimes \vec{u}) = -\nabla p + \nabla\cdot\tau + \overline{\rho}\vec{g} - \overline{\rho}K_C\left[\frac{(1-f_l)^2}{f_l^3 + C_K}\right]\vec{u} + \left\{\sigma\kappa\vec{n} + \frac{d\sigma}{dT}[\nabla T - \vec{n}(\vec{n}\cdot\nabla T)] + 0.54P_0\exp\left[\frac{L_v m}{k_B}\left(\frac{1}{T_v} - \frac{1}{T}\right)\right]\vec{n}\right\}|\nabla\alpha_1| \tag{3}$$

$$\frac{\partial \overline{\rho}\,\overline{c}_e T}{\partial t} + \nabla\cdot(\overline{\rho}\vec{u}\,\overline{c}_e T) = \nabla\cdot(\overline{k}\nabla T) + Q_{laser} - |\nabla\alpha_1|\frac{2\overline{\rho}\,\overline{c}_e}{\rho_1 c_1 + \rho_2 c_2}\left\{h_c(T - T_c) + \sigma_s\varepsilon(T^4 - T_r^4) + 0.82\frac{L_v m}{\sqrt{2\pi m k_B T}}P_0\exp\left[\frac{L_v m}{k_B}\left(\frac{1}{T_v} - \frac{1}{T}\right)\right]\right\} \tag{4}$$

$$\nabla\cdot\vec{u} = 0 \tag{5}$$

here:

$$\overline{\rho} = \alpha_1\rho_1 + \alpha_2\rho_2 \tag{6}$$

$$\tau = 2\overline{\mu}\left[\left(\frac{1}{2}\nabla\vec{u} + \frac{1}{2}(\nabla\vec{u})^T\right) - \frac{1}{3}(\nabla\cdot\vec{u})I\right] \tag{7}$$

$$\vec{n} = \frac{\nabla\alpha_1}{|\nabla\alpha_1|} \tag{8}$$

$$\kappa = -\nabla\cdot\vec{n} \tag{9}$$

where $\overline{\rho}$, ρ_1, ρ_2 are the mixed, metal-phase, and gas-phase densities, respectively, kg/m^3; p is the pressure, Pa; τ is the stress tensor; $\overline{\mu}$ is the

mixed dynamic viscosity, Pa·s; I is the identity matrix; $\vec{g}$ is the gravitational acceleration, m/s^2; K_C is the drag coefficient of the mushy zone [43], 1/s; f_l is the liquid-phase fraction; C_K is a small user-defined value, such as 1×10^{-6}; σ is the temperature-dependent coefficient of surface tension, N/m; κ is the interface curvature, 1/m; $\vec{n}$ is the unit normal vector on the interface; T is the temperature, K; $\frac{d\sigma}{dT}$ is the rate of change of σ with the temperature, N/(m·K); P_0 is the standard atmospheric pressure, Pa; L_v is the gasification latent heat of the metal, J/kg; m is the molecular mass of the metal, kg; k_B is the Boltzmann constant, J/K; T_v is the gasification temperature of the metal, K; $\overline{c}_e$, c_1, c_2 are the equivalent, metal-phase, and gas-phase specific heat capacities, respectively, J/kg; $\overline{k}$ is the mixed thermal conductivity, W/(m·K); Q_{laser} is the laser energy density, W/m^3; h_c is the convective heat transfer coefficient on the interface, W/(m^2·K); T_c is the external convection temperature, K; σ_s is the Stefan-Boltzmann constant, W/(m^2·K^4); ε is the
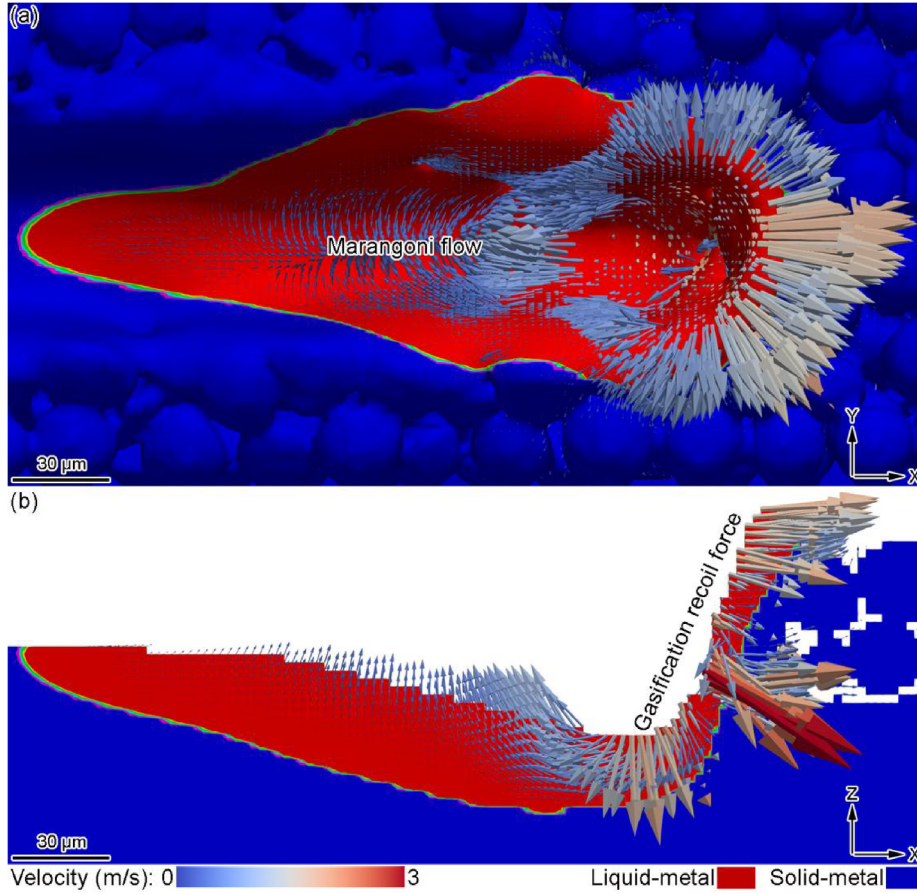
Fig. 6. Molten pool and its velocity distributions at 400 μs: (a) top view; (b) mid-sectional view.

emissivity; and T_r is the external radiation temperature, K.

The right-hand terms in Eq. (3) characterize the effects of the pressure, viscous force, gravity, mushy drag force, surface tension, Marangoni effect, and gasification recoil force on the flow of the molten pool. The right-hand terms in Eq. (4) were used to characterize the effects of heat conduction, laser heating, convection, radiation, and gasification heat dissipation on the heat exchange process of the molten pool. Considering that the laser energy density in the LPBF formation process is extremely high, the use of a surface heat source can easily cause calculation divergence, and the calculation efficiency will be greatly limited. Therefore, the laser energy was applied in the form of a body heat source:

$$Q_{laser} = \frac{f_{\Delta z} q_{laser}}{\Delta z} \tag{10}$$

$$q_{laser} = \frac{2\eta P_{laser}}{\pi R^2} \exp\left(-2\frac{(x - x_0 - vt)^2 + (y - y_0)^2}{R^2}\right) \tag{11}$$

where $f_{\Delta z}$ is the percentage of laser energy occupied by the element; Δz is the element equivalent size, such as the side length of a cube, m; q_{laser} is the surface energy density of the laser, W/m^2; η is the laser absorption rate of the metal; P_{laser} is the laser power, W; R is the radius of the laser spot, m; x, y are the horizontal coordinates of the center point of the element, m; x_0, y_0 are the horizontal coordinates of the center point of the laser spot, m; and v is the scanning speed of the laser, m/s.

Since the shape of the molten pool and the position of the laser spot are constantly changing during the LPBF process, it is necessary to accurately find the elements to which energy is being applied before loading the laser energy. First, the single-layer interface was obtained based on the α_1 information for each element, and then the first-layer elements under the laser action were determined based on the position of the laser spot. Second, based on the first-layer elements, the elements within a certain distance along the direction of gravity were found. Finally, to ensure that the sum of the laser energy percentages of the elements at the same horizontal coordinate was one, the laser energy was distributed based on the metal-phase percentage of each element.

2.3. Prediction process of pore defects

Combined with the above-mentioned theoretical model, the particle distribution of the powder bed was first calculated based on the open-source DEM code Yade. The particle size distribution was Gaussian (the central value was 25 μm, and the variance was 5 μm), the roller speed was 3 mm/s, and the powder bed thicknesses were 50 and 80 μm, respectively. The obtained packing density values corresponding to these powder bed thicknesses were 58.47% and 61.00%, respectively. Based on the open-source CFD code OpenFOAM, the dynamic behavior of the molten pool during the LPBF process was predicted, and the molten pool evolution and influences of various process parameters (laser power, scanning speed, powder bed thickness, and hatch space) on the pore defect were analyzed. The calculation time step was set to 1×10^{-8} s.

3. Results and discussions

3.1. Dimensionless analysis of molten pool evolution

Dimensionless analysis of the molten pool evolution during the LPBF formation process was conducted first, and the geometric model is shown in Fig. 3. The thickness, length, and width of the powder bed were 50, 1000, and 150 μm, respectively, and the substrate thickness was 50 μm. The powder material used was 316L stainless steel, and its
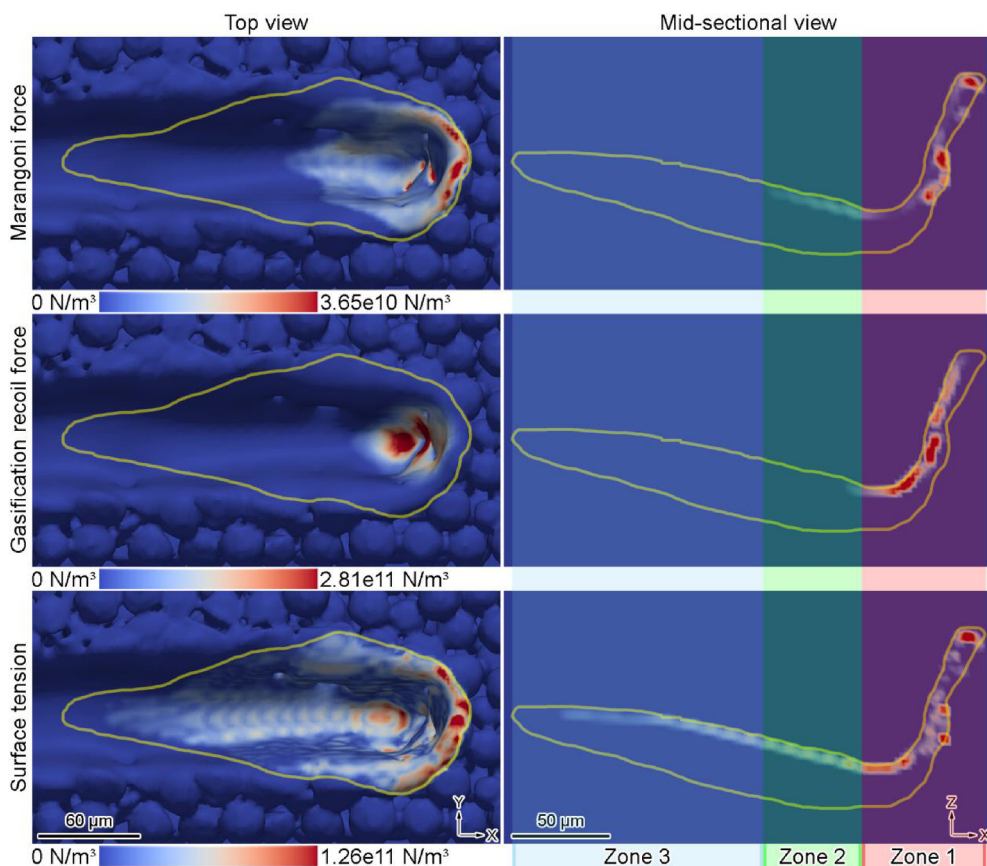
Fig. 7. Distributions of different forces on the molten pool at 400 μs.

Table 3
Typical dimensionless numbers of LPBF molten pool.

Dimensionless number	Definition	Meaning
Peclet number	$Pe = \frac{UL}{\alpha}$	Used to measure the relative importance of convection and diffusion to the heat transfer inside the molten pool [2]
Marangoni number	$Ma = -\frac{d\sigma}{dT}\frac{L\Delta T}{\mu\alpha}$	Used to measure the importance of the Marangoni effect on the molten pool flow [2]
Froude number	$Fr = \frac{U}{\sqrt{gL}}$	Used to measure the importance of gravity on the molten pool flow [44]
Weber number	$We = \frac{\rho L U^2}{\sigma}$	Used to measure the importance of surface tension on the molten pool flow [45]

Note: U is the characteristic velocity of the molten pool, which can be taken as the maximum speed of the molten pool, m/s; L is the characteristic length of the molten pool, which can be taken as the molten pool length, m; α is the thermal diffusivity of the liquid metal, m²/s; ΔT is the difference between the maximum temperature of the molten pool and the solidus temperature of the metal, K; and g is the value of gravitational acceleration, m/s².

alloy composition (mass percentage) was 65.395% Fe, 0.03% C, 1.0% Si, 2.0% Mn, 0.045% P, 0.03% S, 12.0% Ni, 17.0% Cr, 2.5% Mo. Table 1 shows the required material properties calculated by JMatPro v7.0.

Table 2 shows the laser processing parameters. The calculation was a single-track formation process, in which the initial temperature of the metal particles and substrate was 300 K, and the laser moved linearly from the coordinate (50 μm, 75 μm) horizontally to the coordinate (950 μm, 75 μm), then the laser stopped heating, and the system continued to cool for 100 μs.

Figs. 4 and 5 show the top and mid-sectional views, respectively, of the temperature and molten pool distributions at different times, where the Y-direction coordinate of the midsection was 75 μm. The solid-metal particles were gradually heated by the laser to form a molten pool, and the shape of the molten pool was basically stable after a period of time. Due to the extremely high laser energy density, the temperature of the liquid metal in the laser action region was high, which was prone to gasification. Thus, the front part of the molten pool formed a distinct concave shape. As the laser spot moved, the liquid

metal gradually cooled and solidified to form a solidified track. Fig. 6 shows the molten pool and its velocity distributions at a specified time. The velocity distribution shows that the liquid surface in the laser action region exhibited clear downward movement under the influence of the gasification recoil force, while the liquid surface behind the molten pool underwent significant tangential motion under the influence of the Marangoni effect. Therefore, the molten pool evolution during the LPBF process is a result of the combined effects of the Marangoni effect, gasification recoil force, and surface tension.

To quantitatively analyze the influences of the Marangoni effect, gasification recoil force, and surface tension on the flow behavior of the molten pool, Fig. 7 shows the distributions of the different forces experienced by the molten pool at a specified time, and the yellow curve in the figure represents the molten pool boundary. The results show that gasification recoil force mainly acted on the front part of the molten pool, i.e., Zone 1, the Marangoni effect mainly acted on the front and middle parts of the molten pool, i.e., Zones 1 and 2, and the surface tension acted on the entire liquid surface, i.e., Zones 1, 2, and 3.

Table 4
Process parameters for different calculation schemes.

Calculation scheme number	Laser power (W)	Scanning speed (m/s)	Powder bed thickness (µm)	Hatch space (µm)	Length and width of powder bed (µm × µm)	Substrate thickness (µm)
1	50	1.5	50	Single-track formation	1000 × 150	50
2	100	1.5	50	Single-track formation	1000 × 150	50
3	200	1.5	50	Single-track formation	1000 × 150	50
4	250	1.5	50	Single-track formation	1000 × 150	50
5	600	1.5	50	Single-track formation	1000 × 150	150
6	250	3.0	50	Single-track formation	1000 × 150	50
7	200	1.5	80	Single-track formation	1000 × 150	50
8	200	1.5	50	45	1000 × 400	50
9	200	1.5	50	55	1000 × 400	50
10	200	1.5	50	75	1000 × 400	50

From the calculated values, the gasification recoil force in Zone 1 was almost three times the surface tension force and ten times the Marangoni force. Therefore, the liquid surface in Zone 1 was mainly affected by the gasification recoil force, and the downward movement formed a depression. The liquid surface in Zone 2 was mainly affected by the Marangoni and surface tension forces, and the two forces were of the same order of magnitude. However, since the direction of the surface tension force was normal of the liquid surface and the direction of the Marangoni force was tangential, the liquid surface in Zone 2 recovered smoothly along the normal direction under the action of surface tension, and tangential motion occurred under the action of the Marangoni effect. The temperature and its gradient in Zone 3 were low, so the liquid surface in Zone 3 mainly recovered smoothly under the action of surface tension.

To further analyze the effects of different forces on the flow behavior of the molten pool, Table 3 gives the typical dimensionless numbers of the LPBF molten pool. According to the above prediction results, the dimensionless numbers Pe, Ma, Fr, We (defined in Table 3) were roughly 162, 17,886, 63, and 9, respectively. $Pe = 162 >> 1$ means that the heat conduction inside the molten pool was mainly caused by convection, i.e., intense convection occurred inside the molten pool. $Ma = 17886 >> 1$ means that the Marangoni effect had an important influence on the flow behavior of the molten pool. $Fr = 63 > 1$ means that gravity had little effect on the flow behavior of the molten pool. $We = 9 \approx 1$ means that surface tension had an important influence on the flow behavior of the molten pool. Based on the above analysis, the molten pool evolution during the LPBF process was mainly affected by the gasification recoil force, Marangoni effect, and surface tension. The front part of the molten pool formed a depression under the action of the gasification recoil force, the central part underwent intense internal convection under the combined action of Marangoni effect and surface tension, and the back part gradually recovered smoothly under the action of surface tension.

3.2. Influences of process parameters on pore defects

To analyze the influences of the process parameters on pore defects, the LPBF formation processes under different laser powers, scanning speeds, powder bed thicknesses and hatch spaces were calculated. Table 4 lists the process parameters for the different calculation schemes, and the calculation parameters not listed in the table were the same as those in Section 3.1. In addition, the length of the solidified tracks in calculation schemes 1–7 was 900 µm, and the length of the solidified tracks in calculation schemes 8–10 was 825 µm. The cooling time after melting each solidified track was 100 µs.

3.2.1. Influence of laser power on pore defects

To analyze the effect of the laser power on the pore defect during the LPBF process, Figs. 8 and 9 show the prediction results of the solidified tracks for Schemes 1–5. The calculation results of the solidified tracks in Fig. 8 show that when the laser power was low, the depth of the solidified track was small, and the bottom of the solidified track could not be tightly combined with the substrate. The reason was that the applied energy density was low, so that the energy absorbed by the metal particles at the lower end of the powder bed in the formation region was limited. Thus, effectively melting the particles was difficult, which caused pore defects in the bottom of the solidified track due to insufficient fusion. As the laser power increased, the depth of the solidified track gradually increased, and the metal particles in the formation region were effectively melted, forming a dense solidified track that established good metallurgical bonds with the substrate. When the laser power was too large (Fig. 9), the temperature on the laser action region was extremely high, and the region was prone to the "keyhole" effect, which is similar to that in high-power laser welding processes. Gas entrapment occurred in the complex molten pool flow process, and if the gas could not escape in time, pore defects occurred inside the
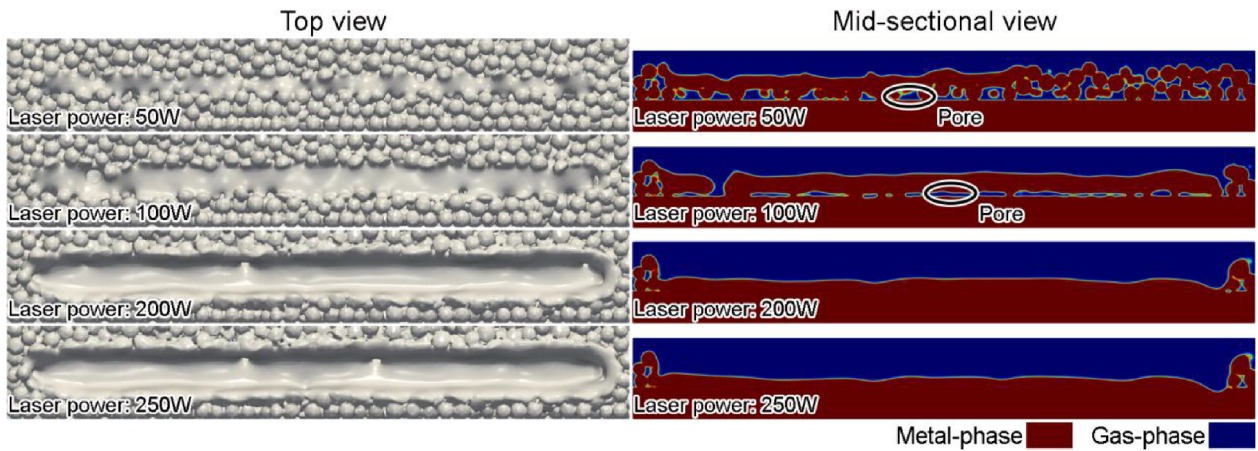
Fig. 8. Top and mid-sectional views of the solidified tracks under different laser powers.
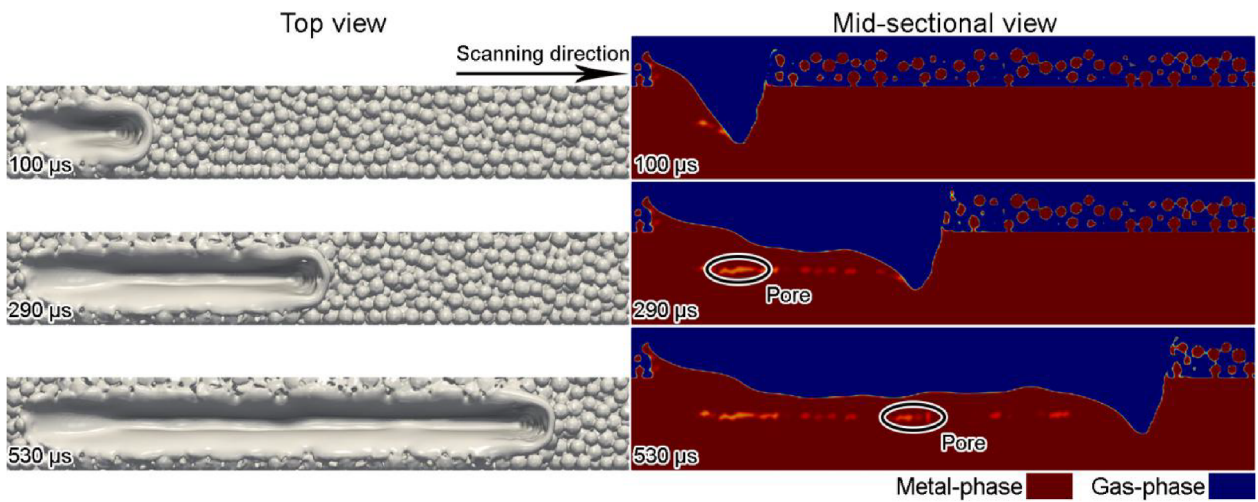

Fig. 9. Top and mid-sectional views of the solidified track at different times under a laser power of 600 W (the pink area is the mixture of the metal and gas phases).
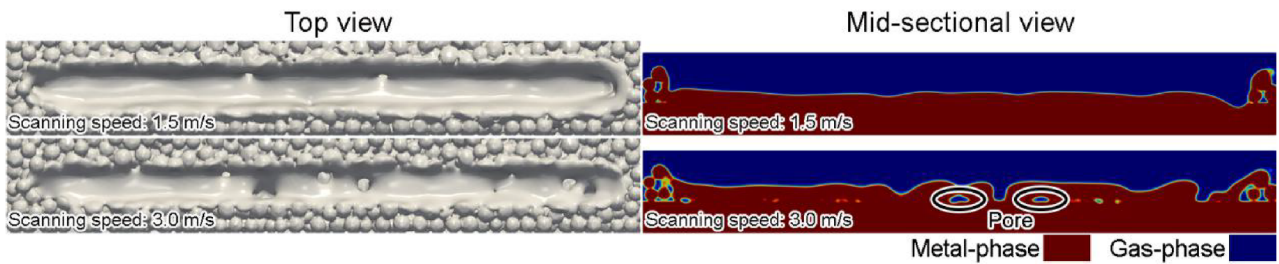

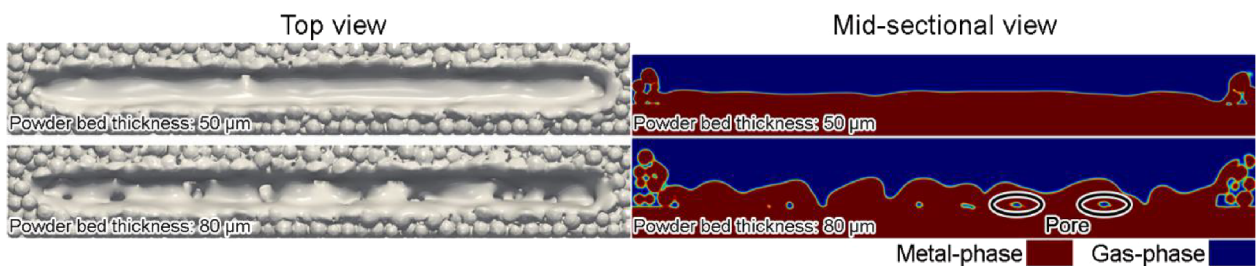**Fig. 10.** Top and mid-sectional views of the solidified tracks under different scanning speeds.

Fig. 11. Top and mid-sectional views of the solidified tracks for different powder bed thicknesses.
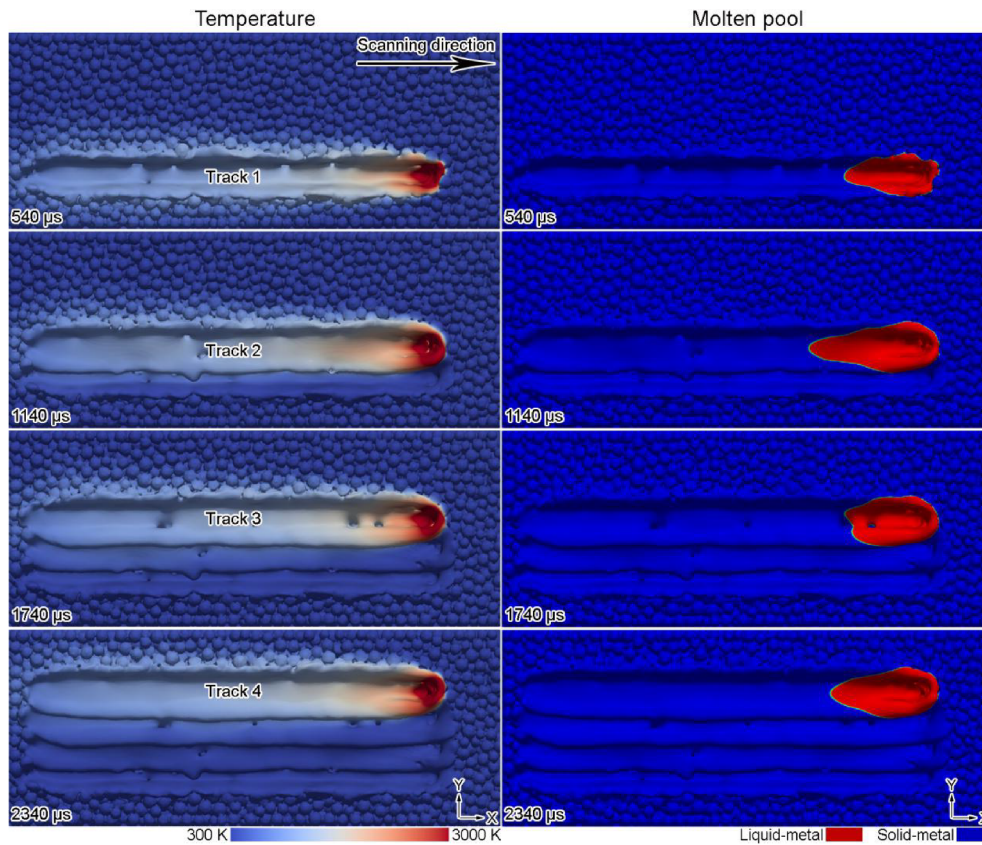
Fig. 12. Temperature and molten pool distributions in LPBF formation zone at different times when the hatch space was 55 μm (top view).
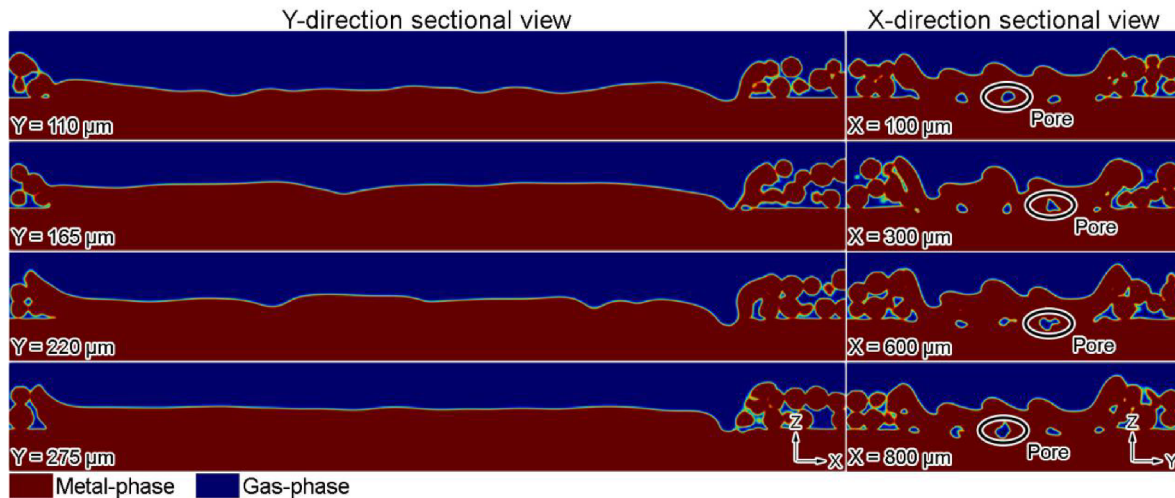

Fig. 13. Sectional views of the final formation zone at hatch space of 55 μm.

solidified track. Therefore, when the laser power was too low, the bottom of the solidified track could contain pore defects due to insufficient fusion, and when the laser power was too high, pore defects would occur inside the solidified track because the entrained gas could not escape in time.

3.2.2. Influence of scanning speed on pore defects

To analyze the effect of the scanning speed on the pore defect, Fig. 10 shows the predicted solidified tracks for Schemes 4 and 6. When the scanning speed was large, the depth of the solidified track was small, and the bottom of the solidified track could not form a tight bond with the substrate. The reason for this is that the energy applied to the

powder bed per unit time was small in this case, and the metal particles at the powder bed bottom in the formation zone could not be effectively melted, thereby causing pore defects at the bottom of the solidified track due to insufficient fusion. Therefore, when the scanning speed was too large, the bottom of the solidified track could contain pore defects due to insufficient fusion, and when the scanning speed was too small, the LPBF formation efficiency could be too low.

3.2.3. Influence of powder bed thickness on pore defects

To analyze the effect of the powder bed thickness on the pore defect, Fig. 11 shows the predicted solidified tracks for Schemes 3 and 7. When the powder bed thickness was large, the solidified track bottom could
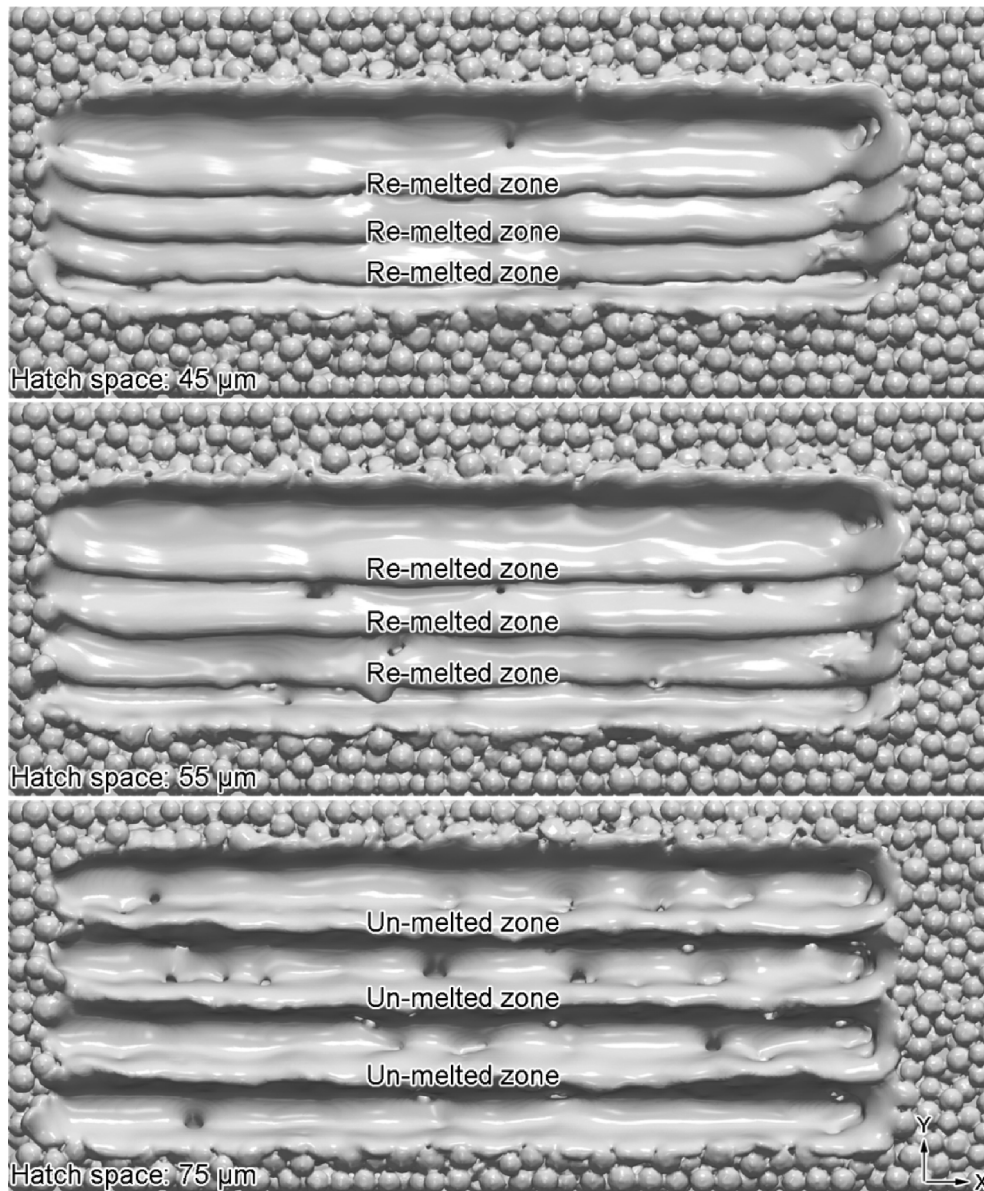
Fig. 14. Top views of solidified tracks for different hatch spaces.

not form a tight bond with the substrate. The thicker powder bed meant that the formation zone needed to absorb more energy to ensure that all the metal particles effectively melted. When the applied laser energy remained unchanged as the powder bed thickness was increased, pore defects could occur due to insufficient fusion at the bottom of the solidified track. Therefore, when the powder bed thickness was too large, the bottom of the solidified track could contain pore defects due to insufficient fusion, and when the powder bed thickness was too small, the LPBF formation efficiency could be too low.

3.2.4. Influence of hatch space on pore defects

To analyze the influence of the hatch space on the pore defect in the LPBF process, the LPBF multi-track formation processes for Schemes 8–10 were predicted. Four solidified tracks were formed in each case, and the scanning direction was always in the positive X-direction. Because the length of each solidified track was only 825 μm, which is much smaller than the solidified track length in actual LPBF production, the temperature of the formation zone was set to 300 K before forming each solidified track during the numerical calculation. Fig. 12 shows the temperature and molten pool distributions in the LPBF formation zone

at different times when the hatch space was 55 μm. Since the particle distribution in the powder bed was random, it was apparent that there were differences in the shapes of the molten pools when the four tracks were formed, but they remained substantially raindrop-like. During the formation process of Tracks 2–4, since one side of the laser action region was a formed solidified track, part of the formed solidified track was re-melted, which facilitated good metallurgical bonds between adjacent solidified tracks. Fig. 13 shows the sectional views of the final formation zone for a hatch space of 55 μm, wherein the four cross-sections along Y-axis were the midsections of the four solidified tracks. Based on the mid-sectional results of the four solidified tracks, there were no pores inside the solidified tracks, but from the results of the four X-direction cross-sections, pores appeared between adjacent solidified tracks and were distributed at the bottom of the powder bed. The reason for the occurrence of the pore defect here was that the laser energy density exhibited a Gaussian distribution in the horizontal plane, i.e., the energy density around the laser action region was low, so that the molten pool shape on the YZ plane was a semi-elliptical distribution. This tended to prevent the adjacent solidified tracks from establishing good connections at the bottom, and pore defects occurred.
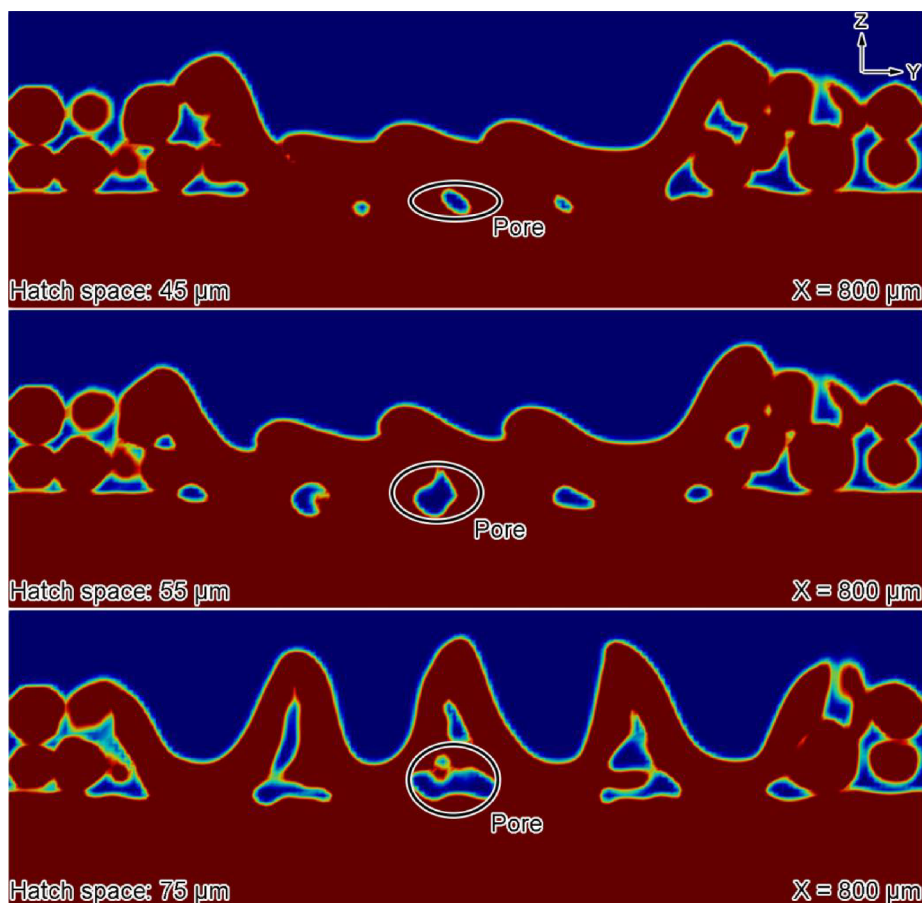
Fig. 15. X-direction sectional views of the formation zone for different hatch spaces.

Fig. 14 shows the top views of the solidified tracks for different hatch spaces. When the hatch space was small (45 μm), the adjacent solidified tracks established good metallurgical bonds. However, the re-melted zone was too large, which tended to reduce the formation efficiency. When the hatch space was large (75 μm), a distinct un-melted zone appeared between the adjacent solidified tracks. Fig. 15 shows the X-direction sectional views of the formation zone for different hatch spaces. Based on the calculation results, pores appeared in all three calculation schemes, and as the hatch space increased, the pore defect between the adjacent solidified tracks became more evident. On the one hand, it was difficult to account for the possible movement of metal particles in the LPBF numerical calculation, such as the liquid metal flow driving the metal particles to move. On the other hand, the temperature of the formation zone was set to 300 K before forming each solidified track, and it was difficult to completely eliminate the pore defect between the adjacent solidified tracks in the prediction result, but the behaviors predicted by the simulation were reasonable. In summary, when the hatch space was large, pore defects could occur due to insufficient fusion of adjacent solidified tracks, and when the hatch space was small, the re-melted zone was too large, which tended to reduce the formation efficiency.

3.2.5. Influence of volumetric energy density on pore defects

The influences of the laser power, scanning speed, powder bed thickness, and hatch space on the pore defect in the LPBF formation process were calculated and analyzed. To comprehensively consider the influences of the process parameters on the pore defect, the volumetric energy density $E_v = P/(v \cdot h \cdot t)$ [46] was introduced, where P is the laser power, W; v is the scanning speed, m/s; h is the hatch space, m; and t is the powder bed thickness, m. E_v was used to characterize the energy absorbed by the powder bed per unit volume during the LPBF process.

Combined with the above simulation results, it can be found that when the volumetric energy density was too small, i.e., when the laser power was too low, the scanning speed was too fast, the powder bed thickness was too large, or the hatch space was too large, the formation zone could contain pore defects due to insufficient fusion of the metal particles. Fig. 16 shows the experimental results of the influences of different process parameters on pore defects [47], and Table 5 shows the energy densities of the simulated cases in Fig. 16. The results confirmed that too small of a volumetric energy density caused pore defects. When the volumetric energy density was too large, the specific situation needed to be analyzed individually. In the case where the laser power was too high, the inside of the solidified track could contain pore defects because the entrained gas could not escape in time, which is common in high-power laser welding processes. In cases when the scanning speed was too low, the powder bed thickness was too small, or the hatch space was too small, the LPBF formation efficiency tended to be too low. In summary, when the volumetric energy density was too small, pore defects could occur due to insufficient fusion of metal particles, and when the volumetric energy density was too large to cause the "keyhole" effect, pore defects could occur because the entrained gas could not escape in time.

4. Conclusions

(1) Using the open-source DEM code Yade and CFD code OpenFOAM, the particle distribution of the powder bed and the pore evolution process at the mesoscopic scale during the LPBF process were predicted. The thermal–force factors affecting the molten pool included the surface tension, Marangoni effect, gasification recoil force, and mushy drag force. The laser energy model used a body heat source based on interface tracking.
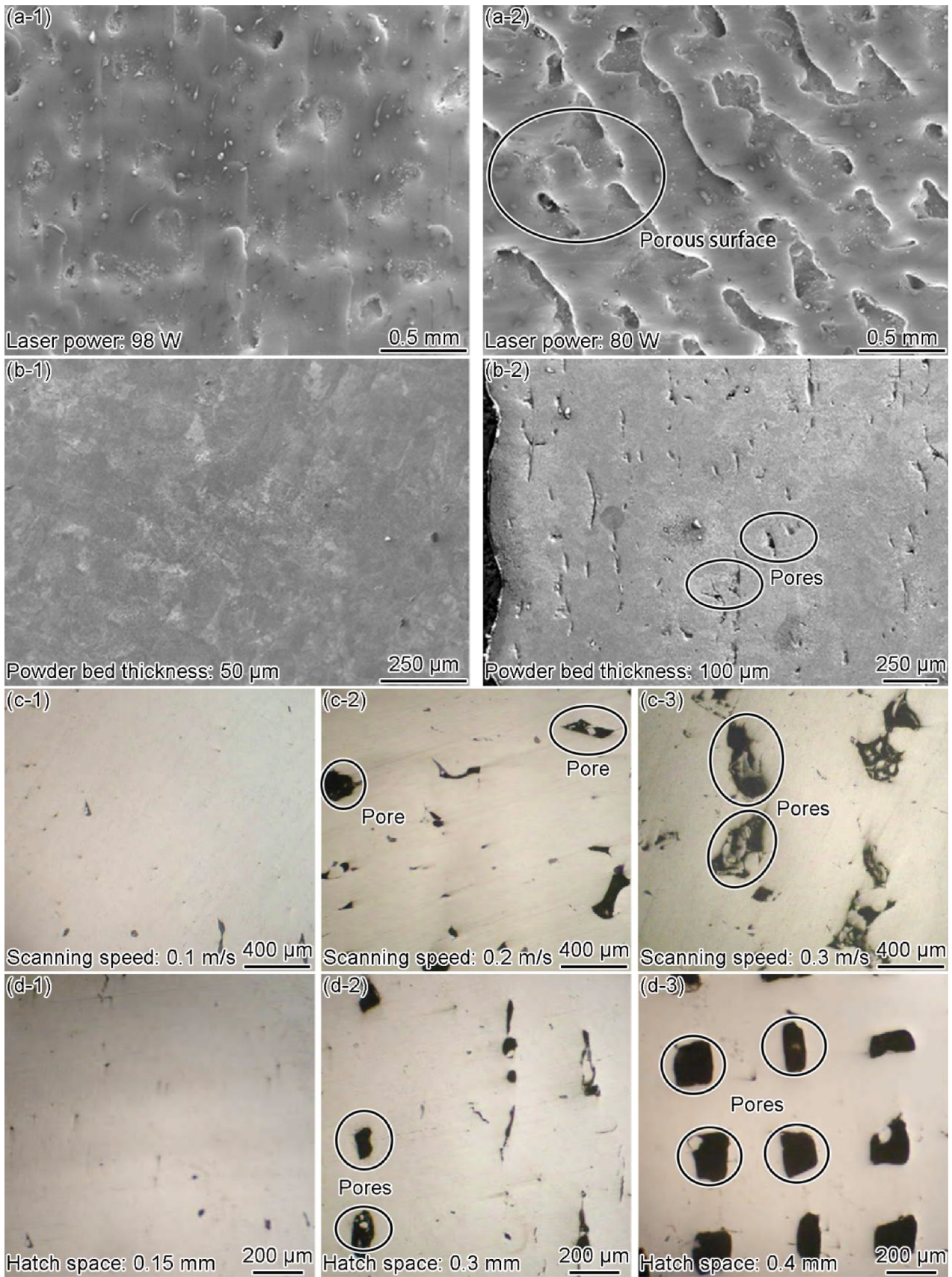
Fig. 16. Influences of different process parameters on pore defects of LPBF components [47]: (a) laser power; (b) powder bed thickness; (c) scanning speed; (d) hatch space.

Table 5
Energy densities of the simulation cases shown in Fig. 16.

Simulation case	Laser power (W)	Scanning speed (m/s)	Powder bed thickness (μm)	Hatch space (μm)	Energy density (J/m^3)
a-1	98	0.09	100	50	2.18×10^{11}
a-2	80	0.09	100	50	1.78×10^{11}
b-1	190	0.1	150	50	2.53×10^{11}
b-2	190	0.1	150	100	1.27×10^{11}
c-1	190	0.1	150	50	2.53×10^{11}
c-2	190	0.2	150	50	1.27×10^{11}
c-3	190	0.3	150	50	8.44×10^{10}
d-1	190	0.1	150	50	2.53×10^{11}
d-2	190	0.1	300	50	1.27×10^{11}
d-3	190	0.1	400	50	9.50×10^{10}

(2) The molten pool evolution during the LPBF process was mainly affected by the gasification recoil force, Marangoni effect, and surface tension. The front part of the molten pool formed a depression under the action of the gasification recoil force, the central part underwent intense internal convection under the combined action of the Marangoni effect and surface tension, and the back part gradually recovered smoothly under the action of surface tension.

(3) When the volumetric energy density was too small, i.e., when the laser power was too low, the scanning speed was too fast, the powder bed thickness was too large, or the hatch space was too large, the formation zone could contain pore defects due to insufficient fusion of the metal particles.

(4) When the volumetric energy density was too large, the specific situation needed to be analyzed. When the laser power was too high, the inside of the solidified track could contain pore defects because the entrained gas could not escape in time. When the scanning speed was too low, the powder bed thickness was too small, or the hatch space was too small, the LPBF formation efficiency tended to be too low.

Declaration of Competing Interest

The author declare that he has no known competing financial interests or personal relationships that could have appeared to influence the work reported in this paper.

Acknowledgements

References

[1] A. Salmi, F. Calignano, M. Galati, E. Atzeni, Virtual Phys. Prototy. 13 (3) (2018) 191–202.
[2] T. DebRoy, H.L. Wei, J.S. Zuback, T. Mukherjee, J.W. Elmer, J.O. Milewski, A.M. Beese, A. Wilson-Heid, A. De, W. Zhang, Prog. Mater. Sci. 92 (2018) 112–224.
[3] H. Choo, K.L. Sham, J. Bohling, A. Ngo, X.H. Xiao, Y. Ren, P.J. Depond, M.J. Matthews, E. Garlea, Mater. Des. 164 (2019) 107534.
[4] J.R. Poulin, A. Kreitcberg, P. Terriault, V. Brailovski, Int. J. Fatigue 127 (2019) 144–156.
[5] A. Thanki, L. Goossens, R. Mertens, G. Probst, W. Dewulf, A. Witvrouw, S. Yang. In: Proceedings of 9th Conference on Industrial Computed Tomography, Padova, Italy, 2019.
[6] C.L.A. Leung, A. Marussi, R.C. Atwood, M. Towrie, P.J. Withers, P.D. Lee, Nat. Commun. 9 (1) (2018) 1355.
[7] Q.L. Guo, C. Zhan, L.I. Escano, Z. Young, L.H. Xiong, K. Fezzaa, W. Everhart, B. Brown, T. Sun, L.Y. Chen, Acta Mater. 151 (2018) 169–180.
[8] A.A. Martin, N.P. Calta, S.A. Khairallah, J. Wang, P.J. Depond, A.Y. Fong, V. Thampy, G.M. Guss, A.M. Kiss, K.H. Stone, Nat. Commun. 10 (1) (2019) 1987.
[9] A. AlFaify, J. Hughes, K. Ridgway, Rapid Prototyping J. 25 (1) (2019) 162–175.
[10] E. Garlea, H. Choo, C.C. Sluss, M.R. Koehler, R.L. Bridges, X. Xiao, Y. Ren, B.H. Jared, Mat. Sci. Eng. A 763 (2019) 138032.
[11] X.Q. Ni, D.C. Kong, W.H. Wu, L. Zhang, C.F. Dong, B.B. He, L. Lu, K.Q. Wu, D.X. Zhu, J. Mater. Eng. Perform. 27 (7) (2018) 3667–3677.
[12] S.M.H. Hojjatzadeh, N.D. Parab, W.T. Yan, Q.L. Guo, L.H. Xiong, C. Zhao, M.L. Qu, L.I. Escano, X.H. Xiao, K. Fezzaa, Nat. Commun. 10 (1) (2019) 3088.
[13] F. Imani, A. Gaikwad, M. Montazeri, P. Rao, H. Yang, E. Reutzel, J. Manuf. Sci. E 140 (10) (2018) 101009.
[14] M.M. Francois, A. Sun, W.E. King, N.J. Henson, D. Tourret, C.A. Bronkhorst, N.N. Carlson, C.K. Newman, T. Haut, J. Bakosi, Curr. Opin. Solid St. M. 21 (2017) 198–206.
[15] L. Cao, X.F. Yuan, Materials 12 (14) (2019) 2272.
[16] C.C. Tseng, C.J. Li, Int. J. Heat Mass Tran. 134 (2019) 906–919.
[17] D.D. Gu, M. Xia, D. Dai, Int. J. Mach. Tool. Manu. 137 (2019) 67–78.
[18] Y. Zhang, J. Zhang, Addit. Manuf. 28 (2019) 750–765.
[19] S.K. Rauniyar, K. Chou, JOM 71 (3) (2019) 938–945.
[20] S. Shrestha, Y.K. Chou, J. Manuf. Sci. E 141 (10) (2019) 101002.
[21] M. Zheng, L. Wei, J. Chen, Q. Zhang, C.L. Zhong, X. Lin, W.D. Huang, Int. J. Heat Mass Tran. 140 (2019) 1091–1105.
[22] B.Q. Liu, G. Fang, L.P. Lei, W. Liu, Appl. Math. Model. 79 (2020) 506–520.
[23] J.L. Tan, C. Tang, C.H. Wong, Metall. Mater. Trans. A 49 (8) (2018) 3663–3673.
[24] W. Nan, M. Ghadiri, Powder Technol. 342 (2019) 801–807.
[25] L. Cao, Int. J. Adv. Manuf. Tech. 105 (2019) 2253–2269.
[26] S.A. Khairallah, A.T. Anderson, A. Rubenchik, W.E. King, Acta Mater. 108 (2016) 36–45.
[27] S. Shrestha, K. Chou. In: Proceedings of 28th Annual International Solid Freeform Fabrication (SFF) Symposium, Austin, USA, 2017.
[28] M.J. Xia, D.D. Gu, G.Q. Yu, D.H. Dai, H.Y. Chen, Q.M. Shi, Int. J. Mach. Tool Manuf. 116 (2017) 96–106.
[29] C. Panwisawas, C.L. Qiu, M.J. Anderson, Y. Sovani, R.P. Turner, M.M. Attallah, J.W. Brooks, H.C. Basoalto, Comp. Mater. Sci. 126 (2017) 479–490.
[30] Z.K. Wang, W.T. Yan, W.K. Liu, M.B. Liu, Comput. Mech. 63 (4) (2019) 649–661.
[31] L. Cao, Int. J. Heat Mass Tran. 141 (2019) 1036–1048.
[32] K.Q. Le, C. Tang, C.H. Wong, Int. J. Therm. Sci. 145 (2019) 105992.
[33] M. Zheng, L. Wei, J. Chen, Q. Zhang, J.Q. Li, S. Sui, G. Wang, W.D. Huang, Appl. Surf. Sci. 496 (2019) 143649.
[34] Z. Wang, M. Liu, J. Mater. Process. Tech. 273 (2019) 116238.
[35] Q. Han, H. Gu, R. Setchi, Powder Technol. 352 (2019) 91–102.
[36] C. Tang, J.L. Tan, C.H. Wong, Int. J. Heat Mass Trans. 126 (2018) 957–968.
[37] M. Bayat, S. Mohanty, J.H. Hattel, Int. J. Heat Mass Trans. 139 (2019) 95–114.
[38] M. Bayat, A. Thanki, S. Mohanty, A. Witvrouw, S. Yang, J. Thorborg, N.S. Tiedje, J.H. Hattel, Addit. Manuf. 30 (2019) 100835.
[39] K.H. Leitz, C. Grohs, P. Singer, B. Tabernig, A. Plankensteiner, H. Kestler, L.S. Sigl, Int. J. Refract. Met. H. 72 (2018) 1–8.
[40] E.J.R. Parteli, T. Pöschel, Powder Technol. 288 (2016) 96–102.
[41] K. Epifancev, A. Nikulin, S. Kovshov, S. Mozer, I. Brigadnov, Am. Mech. Eng. 1 (3) (2013) 73–75.
[42] L. Cao, D.M. Liao, F. Sun, T. Chen, Int. J. Adv. Manuf. Tech. 94 (2017) 807–815.
[43] L. Cao, F. Sun, T. Chen, Z.H. Teng, Y.L. Tang, D.M. Liao, Acta Metall. Sin. 53 (11) (2017) 1521–1531.
[44] R.M. Alexander, Physiol. Rev. 69 (4) (1989) 1199–1227.
[45] P. Day, A. Manz, Y. Zhang: Springer Science & Business Media, 2012.
[46] H. Shipley, D. McDonnell, M. Culleton, R. Coull, R. Lupoi, G. O'Donnell, D. Trimble, Int. J. Mach. Tool. Manuf. 128 (2018) 1–20.
[47] R. Li, Y. Shi, Z. Wang, L. Wang, J.H. Liu, W. Jiang, Appl. Surf. Sci. 256 (13) (2010) 4350–4356.